J. Am. Chem. Soc. **1997,** *119,* 4043−4049

Electronic Band Structure Study of the Anomalous Electrical and Superconducting Properties of Hexagonal Alkali Tungsten Bronzes A_xWO_3 (A = K, Rb, Cs)

Kwang-Soon Lee,[†] Dong-Kyun Seo,[‡] and Myung-Hwan Whangbo*,[‡]

*Contribution from the Departments of Chemistry, The Catholic University of Korea,
Puchon, Kyonggi-Do, South Korea 422-743, and North Carolina State University,
Raleigh, North Carolina 27695-8204*

Received December 30, 1996[⊗]

Abstract: The electrical and superconducting properties of hexagonal alkali tungsten bronzes A_xWO_3 (A = K, Rb, Cs) were examined by calculating the electronic band structure of a representative hexagonal tungsten bronze and analyzing reported crystal structures of A_xWO_3 (A = K, Rb, Cs). These bronzes possess one-dimensional (1D) and three-dimensional Fermi surfaces. The metal-to-semiconductor-to-metal transitions and superlattice reflections in K_xWO_3 and Rb_xWO_3 are explained by a charge density wave (CDW) associated with the 1D Fermi surface. There occurs a maximum in the plots of the CDW onset temperature T_B versus x for K_xWO_3 and Rb_xWO_3. The presence of this maximum and the absence of a CDW in Cs_xWO_3 reflect the balance of two opposing energy factors, the electronic instability and lattice stiffness, in forming a CDW. The dependence of the superconducting transition temperature T_C on x suggests that a CDW transition removes lattice phonons conducive for superconductivity.

1. Introduction

The structures and physical properties of hexagonal alkali tungsten bronzes A_xWO_3 (A = K, Rb, Cs; $\mathrm{O} < x < {}^1/_3$) have been the subject of numerous studies.[1−23] These bronzes have a three-dimensional (3D) WO_3 lattice made up of corner-sharing WO_6 octahedra, and the alkali cations A^+ are located in the hexagonal tunnels of the lattice.[1−14] Thallium and indium tungsten bronzes, $Tl_{0.30}WO_3$ and $In_{0.30}WO_3$,[5,24] are isostructural with the hexagonal alkali tungsten bronzes, but other alkali tungsten bronzes Li_xWO_3 and Na_xWO_3[25] belong to a different structural type and are isostructural with cubic hydrogen tungsten bronze D_xWO_3.[26] The maximum x value of ${}^1/_3$ in A_xWO_3 (A = K, Rb, Cs) results when all the alkali atom sites in the hexagonal tunnels are occupied. The t_{2g}-block bands of the WO_3 lattice become partially filled by the electrons donated from the alkali atoms, which renders metallic properties to A_xWO_3 (A = K, Rb, Cs).

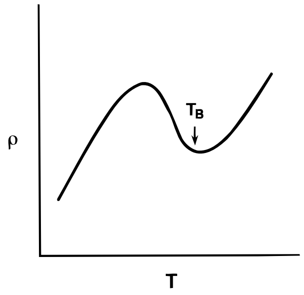

Figure 1. Schematic diagram of an electrical resistivity ρ versus temperature T which shows a metal-to-semiconductor-to-metal phase transition. T_B represents the onset temperature of the metal-to-semiconductor transition.

The hexagonal tungsten bronzes exhibit puzzling electrical and superconducting properties.[15−23] K_xWO_3 and Rb_xWO_3 show a metal-to-semiconductor-to-metal phase transition (Figure 1) in their electrical resistivity along the crystallographic c-direction,[18,20] but not along the directions perpendicular to the c-direction.[20,21] The metal-to-semiconductor phase transition in A_xWO_3 (A = K, Rb) reduces the density of the carriers responsible for the electrical conduction along the c-direction,

---

[†] The Catholic University of Korea.

[‡] North Carolina State University.

[⊗] Abstract published in *Advance ACS Abstracts,* April 15, 1997.

(1) Magneli, A. *Acta Chem. Scand.* **1953**, *7*, 315.

(2) Galasso, F.; Darby, W. *J. Phys. Chem.* **1964**, *68*, 1253.

(3) Goodman, P. *Acta Crystallogr.* **1976**, *B32*, 3280.

(4) Hussain, A.; Kihlborg, L.; Klug, A. *J. Solid State Chem.* **1978**, *25*, 189.

(5) Labbé, Ph.; Goreaud, M.; Raveau, B.; Monier, J. C. *Acta Crystallogr.* **1978**, *B34*, 1433.

(6) Kihlborg, L.; Hussain, A. *Mater. Res. Bull.* **1979**, *14*, 667.

(7) Pye, M. F.; Dickens, P. G. *Mater. Res. Bull.* **1979**, *14*, 1397.

(8) Krause, H. B.; Moulton, W. G.; Morris, R. C. *Acta Crystallogr.* **1985**, *B41*, 11.

(9) Schultz, A. J.; Horiuchi, H.; Krause, H. B. *Acta Crystallogr.* **1986**, *C42*, 641.

(10) Kudo, T.; Oi, J.; Kishimoto, A.; Inoue, H. *Solid State Ionics* **1990**, *40/41*, 567.

(11) Driouiche, A.; Abraham, F.; Touboul, M.; Figlarz, M. *Mater. Res. Bull.* **1991**, *26*, 901.

(12) Kudo, T.; Oi, J.; Kishimoto, A.; Hiratani, M. *Mater. Res. Bull.* **1991**, *26*, 779.

(13) Prinz, H.; Müller, U.; Ha-Eierdanz, M.-L. *Z. Anorg. Allg. Chem.* **1992**, *609*, 95.

(14) Oi, J.; Kishimoto, A.; Kudo, T. *J. Solid State Chem.* **1993**, *103*, 176.

(15) Sienko, M. J.; MacEnness Morehouse, S. *Inorg. Chem.* **1963**, *2*, 485.

(16) Wanlass, D. R.; Sienko, M. J. *J. Solid State Chem.* **1975**, *12*, 362.

(17) Stanley, R. K.; Skokan, M. R.; Morris, R. C.; Moulton, W. G. *Solid State Commun.* **1976**, *19*, 555.

(18) Stanley, R. K.; Morris, R. C.; Moulton, W. G. *Phys. Rev.* **1979**, *B20*, 1903.

(19) Skokan, M. R.; Moulton, W. G.; Morris, R. C. *Phys. Rev.* **1979**, *B20*, 3670.

(20) Cadwell, L. H.; Morris, R. C.; Moulton, W. G. *Phys. Rev.* **1981**, *B23*, 2219.

(21) Sato, M.; Grier, B. H.; Shirane, G.; Fujishita, H. *Phys. Rev.* **1982**, *B25*, 501.

(22) Sato, M.; Fujishita, H.; Moodenbaugh, A. R.; Hoshino, S.; Grier, B. H. *Physica* **1983**, *B + C 120*, 275.

(23) Sato, M.; Grier, B. H.; Fujishita, H.; Hoshino, S.; Moodenbaugh, A. R. *J. Phys. C: Solid State Phys.* **1983**, *16*, 5217.

(24) Swanson, A. B.; Anderson, J. S. *Mater. Res. Bull.* **1968**, *3*, 149.

(25) Wiseman, P. J.; Dickens, P. G. *J. Solid State Chem.* **1976**, *17*, 91.

(26) Wiseman, P. J.; Dickens, P. G. *J. Solid State Chem.* **1973**, *6*, 374.

S0002-7863(96)04455-1 CCC: $14.00

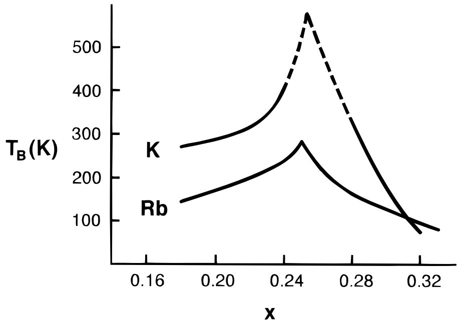

Figure 2. CDW onset temperature T_B as a function of x in K_xWO_3 and Rb_xWO_3 (adapted from ref 20).

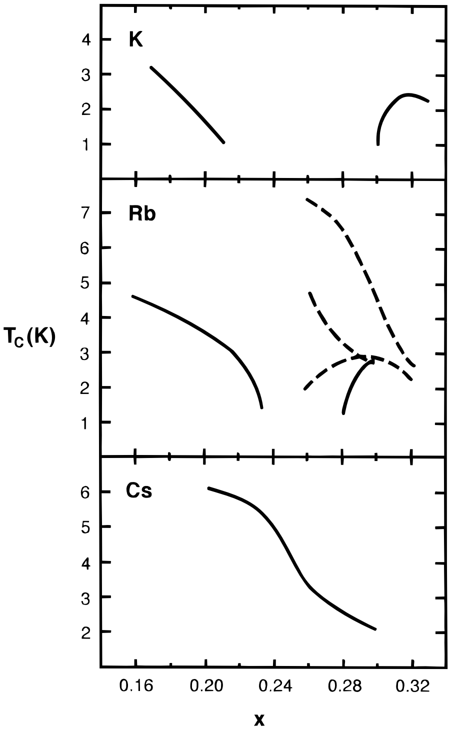

Figure 3. Superconducting transition temperature T_C as a function of x in K_xWO_3, Rb_xWO_3, and Cs_xWO_3 (adapted from ref 20). The T_C-versus-x relationships determined for the region $x > 0.26$ in four separate studies are all different, probably because sample qualities were different. Nevertheless, they all agree in that the region of no superconductivity around $x = 0.25$ is much narrower in Rb_xWO_3 than in K_xWO_3.

because Hall effect studies of Rb_xWO_3 show that the phase transition is accompanied by a large increase in Hall coefficient R_H.[18] In sharp contrast, such a resistivity anomaly as found for K_xWO_3 and Rb_xWO_3 is not observed for Cs_xWO_3.[19] The onset temperature T_B (Figure 1) of the metal-to-semiconductor transition in K_xWO_3 and Rb_xWO_3 depends on x, the T_B-versus-x plots show a maximum around $x = 0.25$, and the T_B is higher for K_xWO_3 than for Rb_xWO_3 at most x values (Figure 2).[18,20] The superconducting properties of A_xWO_3 are also complex (Figure 3). The superconducting transition temperature T_C of Cs_xWO_3 decreases gradually with increasing x.[19] K_xWO_3 and Rb_xWO_3 show no superconductivity in the region of $x = 0.25$, so that their superconductivity occurs in two separate regions of x.[18,20] The region of no superconductivity is much wider in K_xWO_3 than in Rb_xWO_3.

Powder neutron diffraction studies of Rb_xWO_3 show that when the temperature is lowered below T_S, there occur superlattice reflections at **c***/2,[21] which reveals that the unit cell doubles along the c-direction. The T_S-versus-x plot determined for Rb_xWO_3 practically coincides with the corresponding T_B-versus-x plot. Thus, the metal-to-semiconductor phase transition is intimately related to the structural phase transition causing the superlattice reflections. It was suggested that the superlattice reflections arise from the Rb atom ordering in the hexagonal tunnels.[21−23] However, a slightly different picture emerged from single-crystal X-ray and neutron diffraction studies of K_xWO_3.[8,9] The superlattice reflections of K_xWO_3, although they occur at close to **c***/2, are not commensurate and are not explained by the ordering of K atoms.[9]

Transport properties of a metal are described in terms of its Fermi surface.[27−30] The levels of an electronic energy band are described in terms of wave vectors, so the occupied and unoccupied levels of a partially filled band are described by different wave vectors. The Fermi surface of a partially filled band, which is the boundary surface separating the occupied from the unoccupied wave vectors, may consist of several pieces. When a piece of a Fermi surface overlaps another piece when translated by a vector **q**, it is said that the Fermi surface is nested by the vector **q**. A metallic compound with nested Fermi surface has a tendency to lower its electronic energy by undergoing a periodic lattice distortion that opens an energy gap at the Fermi level. This tendency is referred to as a charge density wave (CDW) instability and is a solid-state analog of the first-order Jahn−Teller instability in molecules with incompletely filled degenerate levels. A CDW formation reduces the carrier density at the Fermi level and leads to a metal-to-semiconductor transition. In cases when Fermi surface nesting is incomplete, only the nested portion of Fermi surfaces is removed by the associated CDW formation, thereby causing a metal-to-semiconductor-to-metal transition. The periodic lattice distortion arising from a CDW formation gives rise to superlattice reflections at **q** in diffraction measurements.

So far no electronic band structure study of hexagonal bronzes A_xWO_3 (A = K, Rb, Cs) has been reported, although a cubic sodium bronze, Na_xWO_3, was examined by electronic band structure calculations.[31] Consequently, attempts to explain the physical properties of A_xWO_3 (A = K, Rb, Cs) were not based on their electronic structures. For example, Wanlass and Sienko ascribed the absence of superconductivity in K_xWO_3 and Rb_xWO_3 around $x = 0.25$ to the ordreing of A^+ cation vacancy sites.[16] Others suggested[18−20] that around $x = 0.25$, K_xWO_3 and Rb_xWO_3 undergo a different type of phase transition due to the A^+ cation ordering. In a series of studies, Sato et al.[21−23] emphasized local phonon effects on T_C. Due to the absence of their electronic band structures, the anomalous transport properties of the hexagonal tungsten bronzes A_xWO_3 (A = K, Rb, Cs) have remained unexplained. From the metal-to-semiconductor-to-metal transition, abrupt increase in R_H near the metal-to-semiconductor transition, and superlattice reflections in K_xWO_3 and Rb_xWO_3, it is most likely that these bronzes have a CDW instability along the c-direction. It is important to examine this possibility and a plausible reason why Cs_xWO_3 behaves differently than do K_xWO_3 and Rb_xWO_3. To probe these questions, we calculate the electronic band structure of a representative hexagonal tungsten bronze, $K_{0.26}WO_3$, using the extended Hückel tight binding (EHTB) method[32] and analyze reported crystal structures of A_xWO_3 (A = K, Rb, Cs). The

---

(27) *Physics and Chemistry of Low-Dimensional Inorganic Conductors*; Schlenker, C., Dumas, J., Greenblatt, M., van Smaalen, S., Eds.; Plenum; New York, 1996.

(28) Greenblatt, M. *Acc. Chem. Res.* **1996**, *29*, 219.

(29) Whangbo, M.-H.; Canadell, E. *J. Am. Chem. Soc.* **1992**, *114*, 9587.

(30) Canadell, E.; Whangbo, M.-H. *Chem. Rev.* **1991**, *91*, 1034.

(31) Kopp, L.; Harmon, B. N.; Liu, S. H. *Solid State Commun.* **1977**, *22*, 677.

(32) Whangbo, M.-H.; Hoffmann, R. *J. Am. Chem. Soc.* **1978**, *100*, 6093.

atomic parameters of W and O needed for EHTB calculations were taken from the previous work.[30]

2. Structural Properties

To understand the structures of hexagonal tungsten bronzes A_xWO_3 (A = K, Rb, Cs), it is convenient to describe its ideal structure derived from WO_6 octahedra (**1**). The WO_5 chain (**2a**) is obtained from WO_6 octahedra by sharing their "axial" oxygen (O_{ax}) atoms. A top projection view of a WO_5 chain can be represented by **2b**. In the side projection view **2c**, the plane of the four "equatorial" oxygen atoms (O_{eq}) of each WO_6 octahedron is represented by an $O_{eq}-O_{eq}$ edge. A W_3O_{12} triple-chain **3** results when three WO_5 chains are joined together by sharing their O_{eq} atoms. When W_3O_{12} triple-chains **3** are fused together by sharing their outer O_{eq} atoms, the ideal 3D W_3O_9 lattice **4** is obtained. The outer O_{eq} atoms form hexagonal rings $(O_{eq})_6$, and these rings form hexagonal tunnels along the *c*-direction, where alkali metal atoms A can reside. If an alkali atom is located at the midpoint between every adjacent $(O_{eq})_6$ ring (**5a**), then the resulting 3D lattice has the composition AW_3O_9 per unit cell. This ideal 3D lattice may be referred to as $A_{1/3}WO_3$.

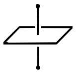
1

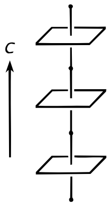

2a


2b

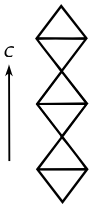

2c

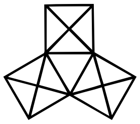
3

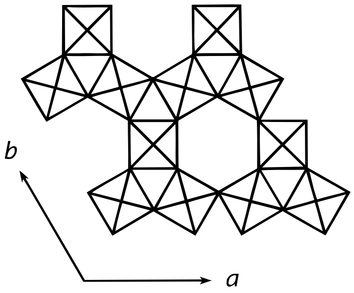

4

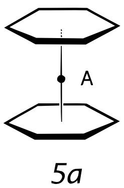

5a

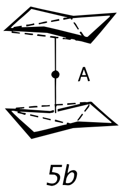

5b

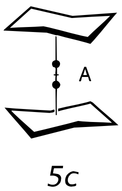

5c

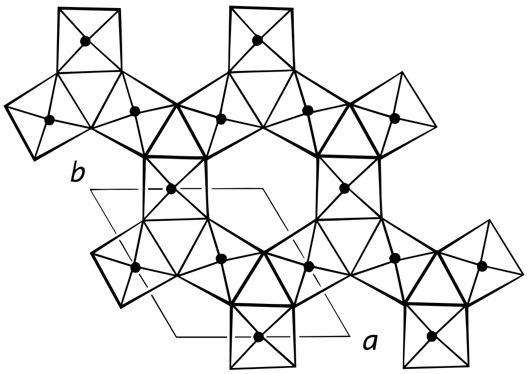

Figure 4. Schematic top view of the tilted WO_6 octahedra in A_xWO_3, where the rhombus represents a unit cell.

Hexagonal tungsten bronzes A_xWO_3[5−7,9] possess structures slightly different from the ideal structure described above. In most cases, the alkali atom sites are not completely occupied, so $x < 1/3$. In the $(O_{eq})_4$ square of a WO_6 octahedron, the W atom is shifted toward one $O_{eq}-O_{eq}$ edge (**6**). In a WO_5 chain, the $(O_{eq})_4$ squares of adjacent WO_6 octahedra are tilted in opposite directions as depicted in **7a**. For six WO_6 octahedra forming a hexagonal ring, the axes of their tilting are arranged as presented in **7b**. Also shown in **7b** are the directions of the W atom shifts within the $(O_{eq})_4$ squares. A schematic top view of the tilted WO_6 octahedra is presented in Figure 4. An important consequence of this tilting is that adjacent $(O_{eq})_6$ rings of a hexagonal tunnel are puckered to adopt "chair" structures (**5b**). Thus, each $(O_{eq})_6$ ring makes three short $O_{eq}\cdots A$ contacts to an adjacent alkali atom A, and the unit cell of the resulting 3D lattice is doubled in size along the *c*-axis direction. As a consequence, hexagonal tungsten bronzes have the formula $A_{6x}W_6O_{18}$ per unit cell.


6

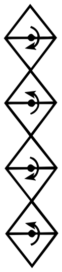
7a

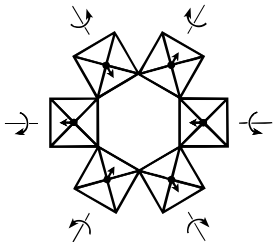
7b

The puckering of adjacent $(O_{eq})_6$ rings allows short $O_{eq}\cdots A$ contacts, thereby providing a more compact packing of O^{2-} anions around each A^+ cation. However, this puckering does not provide an optimum packing for K^+. If a K^+ cation were to occupy the midpoint between the triangular faces of two adjacent puckered $(O_{eq})_6$ rings (hereafter referred to as the symmetrical site), the shortest $K\cdots O_{eq}$ distance would be 3.30 Å,[6] which is significantly longer than the sum of the ionic radii of K^+ and O^{2-} ions. (For example, the ionic radii of K^+, Rb^+, and Cs^+ are 1.37, 1.52, and 1.67 Å, respectively, for six-coordinate sites, and 1.51, 1.61, and 1.74 Å, respectively, for eight-coordinate sites. The ionic radius of O^{2-} is 1.40 Å for the six-coordinate site.[33]) Shorter $K\cdots O_{eq}$ contacts result when

---

(33) Shannon, R. D. *Acta Crystallogr. A* **1976**, *32*, 751.

the K^+ cation is shifted toward one of the two $(O_{eq})_6$ rings. Each K^+ cation can occupy one of the two asymmetrical positions around each symmetrical site (**5c**). When the crystal structure of K_xWO_3 is determined with the space group *P*6₃/*mcm*, which forces each K^+ cation to occupy the symmetrical site, the "temperature" factor *B* for the K^+ position becomes large.[6,7,9] The crystal structure of Cs_xWO_3 determined with the space group $P6_3/mcm$ shows that the temperature factor for Cs^+ is smaller than those for other atoms.[6] Thus the Cs^+ cations occupy the symmetrical sites, which is understandable because Cs^+ is much larger than K^+. The structure of Rb_xWO_3 was also determined with the space group $P6_3/mcm$.[5] This study did not report the temperature factor for the Rb^+ position but concluded that the Rb^+ cations occupy the symmetrical sites based on the electron density map around Rb^+.[5]

The phonon (i.e., lattice vibration) properties of the 3D WO_3 lattice should be influenced by the size of A^+ cations in A_xWO_3. The O−O−O−O dihedral angle of a puckered $(O_{eq})_6$ ring is larger in $K_{0.26}WO_3$ (28.0°)[9] than in $Cs_{0.29}WO_3$ (21.8°),[13] which shows that the puckered $(O_{eq})_6$ rings are more squeezed and flattened in $Cs_{0.29}WO_3$ than in $K_{0.26}WO_3$. When a larger A^+ cation is in the hexagonal tunnel, it fits more tightly with two adjacent puckered $(O_{eq})_6$ rings so that the vibrational motions of the O_{eq} atoms are more restricted, and the WO_3 lattice should become stiffer. The lattice stiffness of A_xWO_3 should also increase as the occupancy of the A^+ cation site increases.

3. Electronic Band Structure

In describing results of our EHTB calculations, it is important to note the orbital interaction patterns leading to the t_{2g}-block bands of a crystal lattice based on corner-sharing WO_6 octahedra.[30] The local coordinate of a WO_6 octahedron can be chosen as in **8**,where the local *z*-axis of a WO_6 octahedron is pointed along the *c*-axis direction of A_xWO_3, so that the t_{2g}-block levels of WO_6 are given by the x^2-y^2, *xz*, and *yz* orbitals. In the t_{2g}-block bands of A_xWO_3 the metal d-orbitals interact primarily with the oxygen p-orbitals in a π-type antibonding manner. The x^2-y^2 orbital does not interact with the O_{ax} p-orbitals (**9a**), but it does with the O_{eq} p-orbitals (**9b**). In contrast, the *xz* and *yz* orbitals interact with the p-orbitals of both O_{ax} and O_{eq} (**10a** and **10b**). Along each corner-sharing octahedral WO_5 chain **2**, the *xz* and *yz* orbitals make π-type interactions, while the x^2-y^2 orbital makes δ-type interactions.

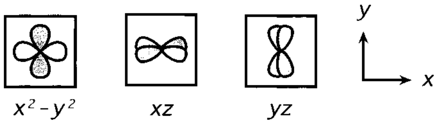

8

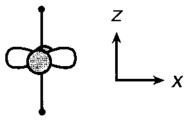

9a

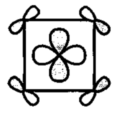

9b

1. Partially Filled t_{2g}-Block Bands. Since A_xWO_3 has the formula $A_{6x}W_6O_{18}$ ($x < 1/3$) per unit cell, the t_{2g}-block bands of A_xWO_3 consist of 18 bands. Given a complete charge transfer from the alkali atoms A to the 3D WO_3 lattice, there are at most two (i.e., 6*x*) electrons per unit cell to fill the t_{2g}-block bands. Therefore, only a few bands lying at the bottom of the t_{2g}-block bands become partially filled. In interpreting the electrical properties of A_xWO_3, it is sufficient to examine these partially filled bands.

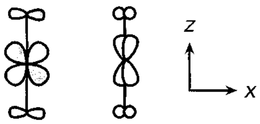

10a

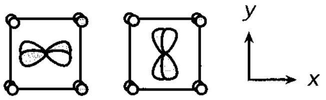

10b

Figure 5 shows the dispersion relations of the bottom portion of the t_{2g}-block bands, which were calculated for the 3D WO_3 lattice taken from the crystal structure of $K_{0.26}WO_3$.[7] The dashed lines of Figure 5 refer to the Fermi levels appropriate for $x = 0.18$, 0.25, and $1/3$. We first consider the ideal case of $x = 1/3$. The band dispersion relations along Γ−Z (i.e., along the *c**-direction) reveal that the bottom three bands are partially filled. The dispersion relations along Γ−X and Γ−M (i.e., in the *a***b**-plane) show that the lowest-lying band (i.e., band a) does not cross the Fermi level, but the other two bands (i.e., bands b and c) do. Consequently, band a is 1D, and bands b and c are 3D, in nature. As *x* decreases from $1/3$ to 0.18, the Fermi level is lowered and eventually cuts band a around the point K = (*a**/3, *b**/3, 0). For $x = 0.18$, therefore, band a deviates from 1D character, while bands b and c keep their 3D character.

The orbital nature of the three partially filled bands can be examined by calculating contributions of the *xz*, *yz*, and x^2-y^2 orbitals to the t_{2g}-block bands. Figure 6 shows plots of the projected density of states calculated for the *xz*/*yz* orbitals (solid line) and for the x^2-y^2 orbital (dotted line), where the dashed lines refer to the Fermi levels appropriate for $x = 1/3$, 0.25, and 0.18. All three partially filled bands associated with $0.18 \le x \le 1/3$ are based on the *xz* and *yz* orbitals, and the x^2-y^2 orbitals contribute to bands lying above the Fermi level. Thus, in hexagonal tungsten bronzes A_xWO_3, it is the π-bands resulting from the *xz* and *yz* orbitals that become partially filled and are responsible for their electrical properties.

2. Fermi Surfaces. Bands b and c lead to 3D Fermi surfaces and hence do not cause a CDW instability. For simplicity, these surfaces are not shown. Figures 7a−c show stereoviews of the Fermi surfaces resulting from band a for $x = 0.18$, 0.25, and $1/3$, respectively. For $x = 0.25$ and $1/3$, this Fermi surface

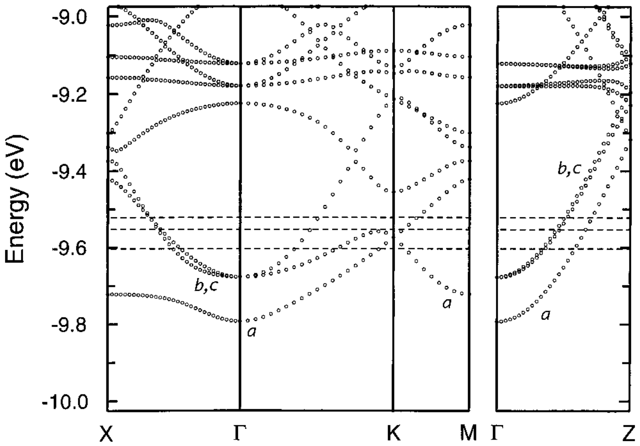

Figure 5. Dispersion relations for the bottom portion of the t_{2g}-block bands of the 3D WO_3 lattice of A_xWO_3. The bottom, middle, and top dashed lines refer to the Fermi levels corresponding to $x = 0.18$, 0.25, and $1/3$, respectively. Γ = (0, 0, 0), X = (*a**/2, 0, 0), K = (*a**/3, *b**/3, 0), M = (*a**/2, *b**/2, 0), and Z = (0, 0, *c**/2).

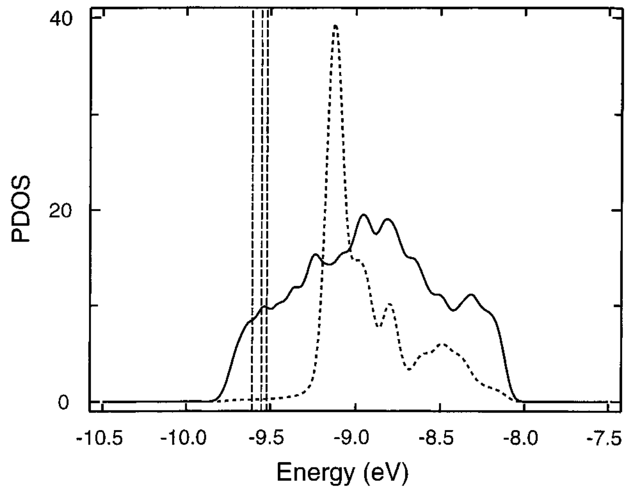

Figure 6. Projected density of state (PDOS) plots calculated for the t_{2g}-block bands of A_xWO_3. The solid curve refers to the *xz*/*yz* orbital contribution and the dotted line to the x^2-y^2 orbital contribution. The left, middle, and right dashed lines refer to the Fermi levels corresponding to $x = 0.18$, 0.25, and $^1/_3$, respectively.

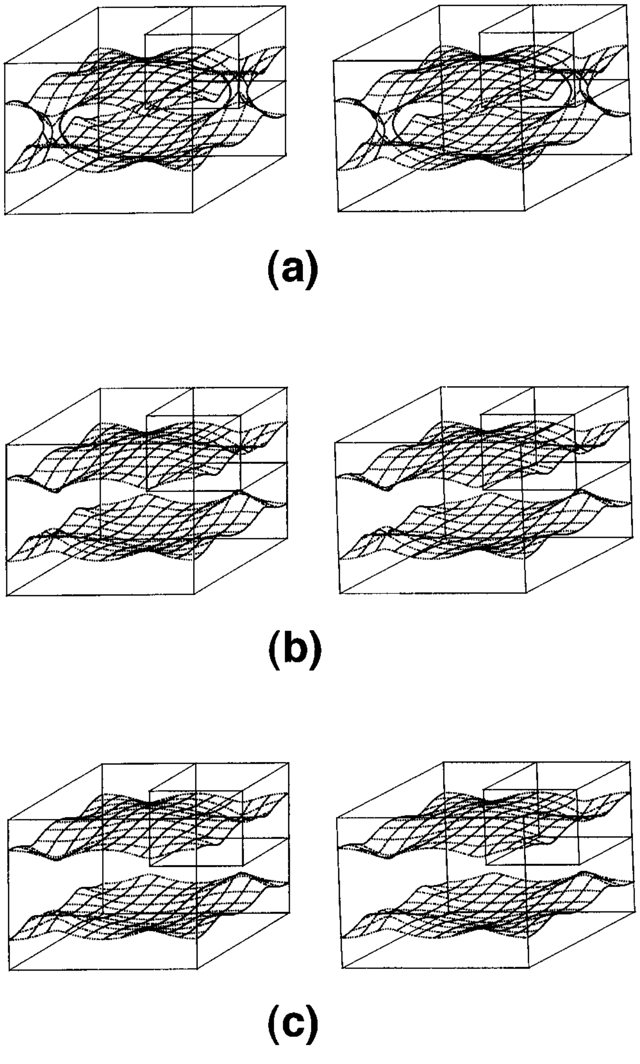

Figure 7. Stereoviews of the 1D Fermi surfaces of A_xWO_3 calculated for $x = 0.18$ (a), 0.25 (b), and $^1/_3$ (c).

consists of two warped sheets perpendicular to the *c**-direction. Thus, band a provides a 1D metallic character along the *c*-direction, as expected from the dispersion relations in Figure 5. As *x* varies from $^1/_3$ to 0.25 to 0.18, the extent of warping increases in the 1D Fermi surface sheets. At $x = 0.18$, the two sheets are merged together around the K point through a funnel-like structure. Thus, the 1D character of band a increases as *x* increases from 0.18 to $^1/_3$. The quasi 1D Fermi surface provides an approximate nesting and can give rise to a CDW instability.[29,30] A flatter Fermi surface has a better nesting and thus a stronger CDW instability. Therefore, the electronic instability favoring a CDW formation (associated with band a) should increase as *x* increases from 0.18 to $^1/_3$ so that the CDW onset temperature T_B should increase gradually with increasing *x*. The prediction is in agreement with experiment when $x < 0.25$, but it is not when $x > 0.25$ (Figure 2). This discrepancy will be discussed further in section 4.1.

As *x* increases from 0.18 to $^1/_3$, the average spacing between the two Fermi surface sheets in Figure 7 increases gradually. The nesting vector **q** determined from the well-nested regions (around X and M) is $\sim 0.5\mathbf{c}^*$ for $x = 0.25$, which gives rise to a nearly "half filled" character for band a. For $x = 0.18$ and $^1/_3$, the nesting vectors can be approximated by $\mathbf{q} = \sim(0.5 - \epsilon)\mathbf{c}^*$ and $\sim(0.5 + \epsilon)\mathbf{c}^*$, respectively, where ϵ is a small positive number.

3. Orbital Nature of the 1D Band. It is of interest to examine why band a has 1D character, because it plays an important role in governing the physical properties of hexagonal tungsten bronzes A_xWO_3 (see section 4). The 3D WO_3 lattice is made up of WO_5 chains, so we first consider a π-band of a WO_5 chain. At $\Gamma = 0$ and $Z = c^*/2$, the metal *xz* (or *yz*) orbitals interact with the O_{ax} p-orbitals as depicted in **11a** and **11b**, respectively. The O_{ax} p-orbitals do not mix with the metal *xz* (or *yz*) orbitals at Γ, but they do in an antibonding manner at Z. Consequently, the energy of this π-band increases as the wave vector varies from Γ to Z (**11c**). This explains the dispersion relations of bands a−c along the Γ−Z direction in Figure 5.

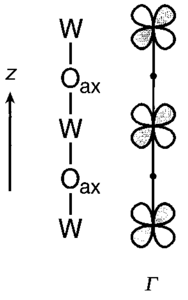

11a

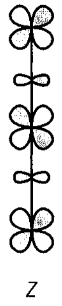

11b

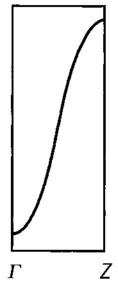

11c

The nodal properties of band a at $\Gamma = (0, 0, 0)$, $X = (a^*/2, 0, 0)$, and $M = (a^*/2, b^*/2, 0)$ are schematically presented in Figures 8a−c, respectively. These diagrams show only the W *xz*/*yz* hybrid orbitals on an *ab*-plane containing the W atoms. The Γ, X, and M points have a common feature that their *c**-components are zero. At these points, therefore, the band orbital in each WO_5 chain of the WO_3 lattice has the orbital pattern **11a**. At $Z = (0, 0, c^*/2)$, $X' = (a^*/2, 0, c^*/2)$, and $M' = (a^*/2, b^*/2, c^*/2)$, the band orbital in each WO_5 chain has the pattern **11b**. Thus band a is dispersive along the *c**-direction (i.e., along Γ−Z, X−X′, and M−M′).

Figures 8a−c show that at Γ, X, and M, every adjacent W *xz*/*yz* hybrid orbital is combined out-of-phase in the W-atom plane. This means that there occurs a node in the vicinity of the O_{eq} position in every $W-O_{eq}-W$ linkage, and the $W-O_{eq}-W$ linkages do not allow an efficient mixing of the O_{eq} p-orbitals.[30] Band a has a similar energy at Γ, X, and M, because the band orbitals are largely composed of the W *xz*/*yz* hybrid orbitals.

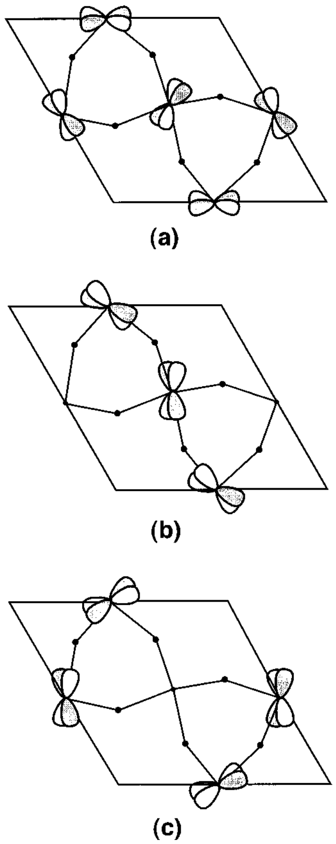

Figure 8. Nodal properties of band a of A_xWO_3 at (a) Γ, (b) X, and (c) M.

Along the Γ−X and X−M directions, the energy of band a changes only slightly, because the W *xz*/*yz* hybrid orbitals cannot mix efficiently with the O_{eq} p-orbitals in the $W-O_{eq}-W$ linkages. As a result, band a becomes much less dispersive along any direction in the a^*b^*-plane (e.g., Γ−X and X−M) than along the c^*-direction. This explains why band a has 1D character.

4. Discussion

1. T_B-versus-*x* Relationships. Our calculations reveal that hexagonal tungsten bronzes A_xWO_3 (A = K, Rb, Cs) have 1D as well as 3D Fermi surfaces. The partially filled 1D band of A_xWO_3 (i.e., band a) is dispersive primarily along Γ−Z, i.e., along the *c*-direction. The metal-to-semiconductor-to-metal transitions in A_xWO_3 (A = K, Rb), found from their electrical resistivity along the *c*-direction, are explained in terms of the CDW formation associated with the 1D Fermi surface. The calculated Fermi surface nesting vector $\mathbf{q} = \sim 0.5\mathbf{c}^*$ is consistent with the observed superlattice reflection peaks of A_xWO_3 (A = K, Rb). However, Cs_xWO_3 does not undergo a CDW transition, although it has a 1D Fermi surface as do K_xWO_3 and Rb_xWO_3. To understand this difference, it is necessary to consider an energy term that disfavors a CDW formation. A CDW formation involves a periodic lattice distortion, which strains the lattice and hence destabilizes it. Thus, a lattice cannot undergo a CDW transition unless the electronic energy gain dominates over the destabilization caused by the lattice strain.[29,34] A CDW formation would be favorable for a system with a soft lattice. As the lattice becomes stiffer, the CDW formation would become less favorable and hence occur at a lower temperature.

Our discussion of the crystal structure of A_xWO_3 (A = K, Rb, Cs) in section 2 suggests that the stiffness of the 3D WO_3 lattice should increase as more alkali atom sites are occupied, and that for a given *x* value, the stiffness of the lattice should increase in the order $K_xWO_3 < Rb_xWO_3 < Cs_xWO_3$. The lack of a CDW transition in Cs_xWO_3 implies that its lattice is too stiff to accommodate a CDW formation. The occurrence of a CDW in K_xWO_3 and Rb_xWO_3 is consistent with the assertion that their lattices are less stiff than that of Cs_xWO_3. Since the WO_3 lattice should be less stiff for K_xWO_3 than for Rb_xWO_3, a CDW formation would be more favorable for K_xWO_3. This explains why the onset temperature T_B of K_xWO_3 is higher than that of Rb_xWO_3 for most *x* values (Figure 2).

In A_xWO_3 the stiffness of the WO_3 lattice should increase with increasing *x* from 0.18 to $^1/_3$. This effect predicts the T_B to decrease gradually as *x* increases. However, as pointed out in section 3.3, the electronic instability associated with the 1D band predicts the T_B to increase gradually as *x* increases from 0.18 to $^1/_3$. That is, the electronic instability and the lattice stiffness have opposing influences on the T_B-versus-*x* relation. The occurrence of a maximum in the T_B-versus-*x* plots (Figure 2) can be considered a consequence of the two opposing effects. Then the electronic instability dominates when $x < 0.25$, while the lattice stiffness does when $x > 0.25$.

The above reasoning provides a natural explanation for the difference and similarity in the slopes of the T_B-versus-*x* curves in Figure 2. In the $x > 0.25$ region, where the lattice stiffness dominates, the slope is much stiffer for K_xWO_3 than for Rb_xWO_3. Since the K^+ ion is smaller than the Rb^+ ion, the lattice stiffness should decrease more rapidly for K_xWO_3 than for Rb_xWO_3 as *x* is decreased from $^1/_3$. Consequently, the slope of the T_B-versus-*x* curve is much stiffer for K_xWO_3 in the $x > 0.25$ region. However, K_xWO_3 and Rb_xWO_3 have similar slopes in the $x < 0.25$ region of the T_B-versus-*x* curves. This is understandable because the electronic instability dominates in this region so that the cation size difference cannot strongly influence T_B.

2. T_C-versus-*x* Relationships. To discuss what structural and electronic factors might be responsible for the T_C-versus-*x* relationships in Figure 3, we assume that the BCS theory of superconductivity[35,36] is applicable to the hexagonal bronzes A_xWO_3 (A = K, Rb, Cs), because the T_C's of these compounds are low. In the BCS theory, a superconducting state is caused by electron−phonon interactions, and the T_C of a superconductor increases with an increase in the electron−phonon coupling constant λ. This constant increases with an increase in the electron density of states at the Fermi level, $n(e_f)$, and also with an increase in the softness of the lattice. A number of studies on organic salt superconductors have shown[37−40] that the occurrence of superconductivity in a metal is prevented when the metal undergoes a CDW formation and when the metal has a random potential in the lattice. In a series of structurally related organic superconducting salts, the T_C is generally found to increase as the lattice becomes softer.

K_xWO_3 and Rb_xWO_3 exhibit no superconductivity for *x* values around 0.25, where these bronzes have the strongest tendency

---

(34) Whangbo, M.-H.; Seo, D.-K.; Canadell, E. ref 27, p 285.

(35) Bardeen, J.; Cooper, L. N.; Schrieffer, J. R. *Phys. Rev.* **1957**, *108*, 1175.

(36) McMillan, W. L. *Phys. Rev.* **1968**, *167*, 331.

(37) Whangbo, M.-H.; Williams, J. M.; Schultz, A. J.; Emge, T. J.; Beno, M. A. *J. Am. Chem. Soc.* **1987**, *109*, 90.

(38) Williams, J. M.; Schultz, A. J.; Geiser, U.; Carlson, K. D.; Kini, A. M.; Wang, H. H.; Kwok, W.-K.; Whangbo, M.-H.; Schirber, J. E. *Science* **1991**, *252*, 1501.

(39) Geiser, U.; Schultz, A. J.; Wang, H. H.; Watkins, D. M.; Stupka, D. L.; Williams, J. M.; Schirber, J. E.; Overmyer, D. L.; Jung, D.; Novoa, J. J.; Whangbo, M.-H. *Physica C* **1991**, *174*, 475.

(40) Williams, J. M.; Ferraro, J. R.; Thorn, R. J.; Carlson, K. D.; Geiser, U.; Wang, H. H.; Kini, A. M.; Whangbo, M.-H. *Organic Superconductors*; Prentice Hall: New York, 1992.

toward a CDW formation. In contrast, Cs_xWO_3 is superconducting in the region of x, where both K_xWO_3 and Rb_xWO_3 show no superconductivity, and it does not exhibit a CDW instability. After a CDW transition, most conducting electrons associated with the warped 1D Fermi surface may be removed. However, this cannot be responsible for the absence of superconductivity in K_xWO_3 and Rb_xWO_3 around $x = 0.25$, because conducting electrons associated with their 3D Fermi surfaces will remain after the CDW formation.

When $x < {}^1/_3$ in A_xWO_3, some A^+ cation sites of the hexagonal tunnels are vacant, and the alkali vacancies are randomly distributed, thereby creating a random potential for conducting electrons. In general, superconductivity is suppressed by a random potential in the lattice. Thus from the disappearance of superconductivity in K_xWO_3 and Rb_xWO_3 around $x = 0.25$, one might speculate that the extent of randomness in the potential is largest around $x = 0.25$. However, this argument is not valid because Cs_xWO_3 is superconducting around $x = 0.25$.

The superconductivity of K_xWO_3 and Rb_xWO_3 can be suppressed around $x = 0.25$, if their CDW formation removes lattice phonons conducive for superconductivity. This argument predicts that a stronger tendency for CDW formation will make it less favorable to form a superconducting state. As already pointed out, around $x = 0.25$, K_xWO_3 has a stronger tendency for CDW formation than does Rb_xWO_3, so that the region of no superconductivity is wider for K_xWO_3. Cs_xWO_3 does not undergo a CDW transition and is therefore superconducting in the region of x, where both K_xWO_3 and Rb_xWO_3 show no superconductivity.

Finally, it is noted that the T_C of Cs_xWO_3 decreases gradually when x increases toward ${}^1/_3$. This trend is understandable, because the stiffness of the WO_3 lattice should increase with increasing x and because the T_C generally decreases as the latrice becomes stiffer.

5. Concluding Remarks

Our electronic band structure calculations show that hexagonal tungsten bronzes A_xWO_3 ($A = K$, Rb, Cs) possess 1D as well as 3D Fermi surfaces. The partially filled 1D band of A_xWO_3 is dispersive mainly along the c-direction. The metal-to-semiconductor-to-metal transitions and superlattice reflections observed for K_xWO_3 and Rb_xWO_3 are explained in terms of a CDW formation associated with the 1D Fermi surface. As x increases from 0.18 to ${}^1/_3$, the quasi-1D Fermi surfaces become flatter, thereby strengthening the electronic instability toward a CDW formation. However, the stiffness of the WO_3 lattice should increase as x is increased and as the cation is changed from K^+ to Rb^+ to Cs^+. The lattice stiffness makes a CDW formation unfavorable and counteracts the effect of the electronic instability. The anomalies in the T_B-versus-x plots are explained by the interplay of the two opposing effects, the lattice stiffness and the electronic instability. The anomalous T_C-versus-x relationships of A_xWO_3 suggest that a CDW transition removes lattice phonons conducive for superconductivity.

Acknowledgment. Work at North Carolina State University was supported by the U.S. Department of Energy, Office of Basic Sciences, Division of Materials Sciences, under Grant No. DE-FG05-86ER45259. Work at The Catholic University of Korea was supported by Grant No. C044677-I and by Grant BSRI-96-3421 from Ministry of Education.

JA964455T